

Hydrothermal activity along the slow-spreading Lucky Strike ridge segment (Mid-Atlantic Ridge): Distribution, heatflux, and geological controls

J. Escartin, T. Barreyre, M. Cannat, R. Garcia, N. Gracias, A. Deschamps, A. Salocchi, P.-M. Sarradin, V. Ballu

▶ **To cite this version:**

J. Escartin, T. Barreyre, M. Cannat, R. Garcia, N. Gracias, et al.. Hydrothermal activity along the slow-spreading Lucky Strike ridge segment (Mid-Atlantic Ridge): Distribution, heatflux, and geological controls. Earth and Planetary Science Letters, 2015, 431, pp.173-185. 10.1016/j.epsl.2015.09.025 . insu-01244343

HAL Id: insu-01244343
https://insu.hal.science/insu-01244343

Submitted on 6 Aug 2020

HAL is a multi-disciplinary open access archive for the deposit and dissemination of scientific research documents, whether they are published or not. The documents may come from teaching and research institutions in France or abroad, or from public or private research centers.

L'archive ouverte pluridisciplinaire **HAL**, est destinée au dépôt et à la diffusion de documents scientifiques de niveau recherche, publiés ou non, émanant des établissements d'enseignement et de recherche français ou étrangers, des laboratoires publics ou privés.

Hydrothermal activity along the slow-spreading Lucky Strike ridge segment (Mid-Atlantic Ridge): Distribution, heatflux, and geological controls

J. Escartin[1*], T. Barreyre[2], M. Cannat[1], R. Garcia[3], N. Gracias[3], A. Deschamps[4*], A. Salocchi[5], P.-M. Sarradin[6], and V. Ballu[7]

[1]Laboratoire de Géosciences Marines, IPGP, CNRS UMR7154, Paris, France

[2]Woods Hole Oceanographic Institution, Woods Hole, MA, USA

[3]VICOROB, University of Girona, Spain

[4]Laboratoire Domaines Océaniques, CNRS & Université de Bretagne Occidentale, Brest, France

[5]University of Modena and Reggio Emilia, Modena, Italy

[6]EEP, IFREMER, Brest, France

[7]Université de La Rochelle, La Rochelle, France

[*]Corresponding author: Javier Escartin – escartin.javier@gmail.com

[*]Note: This article is dedicated to the memory and contributions of the co-author Anne Deschamps, who passed-away in late 2014 during the preparation and writing of this manuscript.

© 2015. This manuscript version is made available under the Elsevier user license
http://www.elsevier.com/open-access/userlicense/1.0/

28 **Abstract**

29 We have reviewed available visual information from the seafloor, and recently acquired
30 microbathymetry for several traverses across the Lucky Strike segment, to evaluate the
31 distribution of hydrothermal activity. We have identified a new on-axis site with diffuse
32 flow, Ewan, and an active vent structure ~1.2 km from the axis, Capelinhos. These sites
33 are minor relative to the Main field, and our total heatflux estimate for all active sites
34 (200-1200 MW) is only slightly higher than previously published estimates. We also
35 identify fossil sites W of the main Lucky Strike field. A circular feature ~200 m in
36 diameter located on the flanks of a rifted off-axis central volcano, is likely a large and
37 inactive hydrothermal edifice, named Grunnus. We find no indicator of focused
38 hydrothermal activity elsewhere along the segment, suggesting that the enhanced melt
39 supply and the associated melt lenses, required to form central volcanoes, also sustain
40 hydrothermal circulation to form and maintain large and long-lived hydrothermal fields.
41 Hydrothermal discharge to the seafloor occurs along fault traces, suggesting focusing of
42 hydrothermal circulation in the shallow crust along permeable fault zones.

43

44 **1. Introduction and geological setting**

45 Hydrothermal activity along mid-ocean ridges controls cooling of the oceanic
46 lithosphere, and impacts its thermal structure and the processes operating there (e.g.,
47 magmatic emplacement, faulting, seismicity, diking and melt delivery to the seafloor).
48 Understanding the distribution of hydrothermal activity and its nature is necessary to
49 quantify the associated heatflux, its partition between diffuse and focus flow
50 recognizable at the seafloor, and to evaluate the amount of cooling with no expression at
51 the seafloor (e.g., conductive cooling or low-temperature, diffuse percolation).

52 Slow spreading ridge sections with significant melt supply typically define linear ridge
53 segments with lengths of a few tens of km to up to ~100 km. These segments typically
54 develop ridge-parallel normal faults on both flanks, and thick crust at their center
55 indicating melt-focusing along-axis. As in the case of the Lucky Strike segment, sustained
56 volcanism may lead to the development of central volcanoes (Escartín et al., 2014). The
57 slow-spreading Lucky Strike segment is unique in that it has been extensively studied
58 during more than two decades, following the discovery of the Lucky Strike hydrothermal
59 field, from hereon referred to as the Main Lucky Strike hydrothermal field (MLSHF),
60 located at its segment center and at the summit of the central volcano (Langmuir et al.,

1997). This is one of the most extensive hydrothermal fields discovered to date, and it is located along a recent graben dissecting the Lucky Strike central volcano (Humphris et al., 2002; Ondréas et al., 2009; Barreyre et al., 2012; Escartín et al., 2014). Water-column studies have also revealed hydrothermal plumes at greater depths than that of the MLSHF (Wilson et al., 1996; German et al., 1996; Thurnherr et al., 2008). These authors proposed a yet unidentified source at the southern end of the segment and at a depth of 2000 m.

A ~3-3.5 km deep magma chamber (Singh et al., 2006) at the base of a ~600 m thick Layer 2A (Seher et al., 2010) underlies The MLSHF (Figure 2). Major faults within the rift valley (Escartín et al., 2014) can be linked to fault reflectors that do not reach the magma chamber depth in seismic reflection profiles (Combier et al., 2015). Microseismicity below the hydrothermal field (Crawford et al., 2013) is unrelated to these fault reflectors, and likely corresponds to hydrothermal cooling instead (Figure 3).

In this paper we provide a synthesis of available information along the Lucky Strike ridge segment, from seafloor observations and imagery to microbathymetric and acoustic data (Figure 1). We analyze these data to identify and map new hydrothermal sites, and use other observables (presence of a magma chamber, microseismicity, faulting) to constrain the processes controling distribution and location of hydrothermal activity along this segment, to re-evaluate heat fluxes at the segment scale, and to discuss the implications for heat extraction and magmatic supply. Finally, we review evidence of hydrothermal activity along the segment based on water-column studies.

2. Data and indicators of hydrothermal activity at the seafloor

The Lucky Strike area has been targeted by numerous cruises in the last 25 years, providing extensive visual information from direct human observations, video imagery, and electronic still-camera images acquired with human-operated vehicles (HOVs), remotely operate vehicles (ROVs), and deep-towed camera systems. These visual observations are complemented with near-bottom high-resolution bathymetry data acquired both with ROVs and Autonomous Underwater Vehicles (AUVs) during cruises in 2008 and 2009, in addition to a prior deep-towed sonar survey (Scheirer et al., 2000; Humphris et al., 2002; Escartín et al., 2014), as summarized in Figure 1 and Supplementary Table 1. Near-bottom ROV and AUV bathymetry data have a resolution of several decimeters to a few meters per pixel, depending on survey altitude, and provide

detailed information on the seafloor texture that can be used to discriminate between hydrothermal structures (e.g., hydrothermal mounds and chimneys, Figure 2) from other structures whose origin is instead volcanic (e.g., hummocks, lava channels and flows), tectonic (e.g., faults, fissures), or related to secondary mass-wasting processes (e.g., landslides along fault scarps).

2.1. Visual observations

The bulk of the field work involving visual observations at the seafloor focuses on the MLSHF, which is yearly visited since 2008 (MoMAR08) and is instrumented for monitoring since 2010 as part of the MOMARSAT European Multidiciplinary Seafloor and water column Observatory (EMSO) deep-sea seafloor observatory (Colaço et al., 2011). In this study we use imagery and visual observations along with HOV, ROV, and deep-towed camera systems (Figure 1a) that extend both along the Lucky Strike segment, and across the full rift valley width (Figure 1a), and present a. large-area seafloor photomosaics from vertically-acquired imagery. The first systematic survey of the MLSHF was conducted with ARGO II towed-camera in 1996 (Humphris et al., 2002; Escartin et al., 2008). Subsequent surveys conducted with the ROV VICTOR low-light camera covered fully the MLSHF (Barreyre et al., 2012), extending beyond prior surveys, and South along the ridge axis (Figure 1). Vertical imagery was processed into a single georeferenced seamless giga-mosaic. Details on the ARGO II and OTUS image surveys at MLSHF, and on image processing and mosaicing are provided elsewhere (Escartín et al., 2008; Barreyre et al., 2012; Prados et al., 2012); here we present for the first time the 2009 photomosaic ~1 km south of the MLSHF.

Active hydrothermal sites are readily identifiable visually from venting fluids (high-temperature black smokers and clear-fluid vents, diffuse outflow at lower temperatures), hydrothermal macrofauna and microbial communities (e.g., bacterial mats and mussel beds), or white anhydrite deposits that require venting temperatures of 120-150°C (Bischoff and Seyfried, 1978). These visual features have been used to extensively map the MLSHF from both photomosaics and oblique-view imagery acquired with ROVs or HOVs (Barreyre et al., 2012). Fossil hydrothermal outflow areas are also recognizable by fossil chimneys, sulfide rubble, and hydrothermal staining, which are clearly distinguishable from basalt or sediment (Lalou et al., 1989; Barreyre et al., 2012).

Supplementary Table 1 and Figure 1 provide an overview of the seafloor visually explored along >900 km of submersible tracks at the Lucky Strike segment, largely concentrated at the segment center and the MLSHF. The seafloor photomosaics

(Barreyre et al., 2012) image ~1.5 km^2 of seafloor centered on the MLSHF, and ~0.4 km^2 on-axis ~2 km south of MLSHF. Seafloor observations outside the MLSHF were conducted primarily during the 1994 DIVA cruise (Fouquet et al., 1994; Ondreas et al., 1997) with both HOV Nautile and Scampi camera tows to the North, during the 2006 Graviluck cruise (HOV and camera tows), and during ROV dives in subsequent cruises (Supplementary Table 1). In this paper the visual indicators of hydrothermal activity are from shipboard observations (cruise reports and published results), and from a systematic review of ROV and HOV video imagery and seafloor photography available to us (cruises underlined in Supplementary Table 1).

2.2. Microbathymetric data

Microbathymetric data acquired in 2006 (MOMARETO cruise, Supplementary Table 1) (Ondréas et al., 2009), was complemented with MOMAR'08 and Bathyluck'09 surveys using ROV VICTOR6000 equipped with a RESON 7150 multibeam system, and AUV Aster-X equipped with a SIMRAD EM2000 multibeam system. After data processing (ping editing, correction of navigation, filtering, and gridding), the final microbathymetric grids have a pixel resolution that varies between 25 cm and 2 m per pixel depending on survey altitude.

The MOMAR'08 and Bathyluck'09 surveys where conducted at the segment center and over the central volcano summit, across the rift valley floor at different locations along the segment, and at the flank of the southwestern inside corner of the segment end (Figure 1). The combined set of microbathymetric surveys, which cover ~35 km^2 of the Lucky Strike segment seafloor, is one of the most extensive microbathymetry surveys along a slow-spreading ridge segment, and complements a prior ~190 km^2 high-resolution sonar survey (Scheirer et al., 2000a; Escartín et al., 2014). For this study we analyzed shaded relief and slope maps of the microbathymetric dataset to identify the seafloor morphology consistent with that of hydrothermal deposits, as described below.

2.3. Acoustic backscatter data

The central portion of the Lucky Strike segment was surveyed with the DSL120 deep-towed, near-bottom high-resolution sonar system (Scheirer et al., 2000; Humphris et al., 2002). These data have been re-processed and presented elsewhere (Escartín et al., 2014), together with an interpretation of the tectonic and volcanic structure of this

portion of the Lucky Strike segment. Sonar data are shifted locally to match the microbathymetry, as the navigation of the DSL120 towed vehicle is less accurate than that of ROV or AUVs used in microbathymetric surveys. By themselves sonar data are not sufficient to identify hydrothermal deposits. First, sulfides do not display acoustic properties that are distinct from basaltic basemen.. Second, acoustic backscatter depends on numerous parameters such as insonification direction and angle, acoustic shading, sedimentation, and instrumental artifacts, among other factors. In this study we only use acoustic backscatter to support the interpretation of the microbathymetric data.

2.4. Identification and extent of hydrothermal sites and fields

Hydrothermal activity with high-temperature fluid discharge ubiquitously displays mounds and chimneys that can reach up to a few tens of meters above surrounding seafloor, with basal widths of meters to a few tens of meters (Figure 2). Areas with hydrothermal vents have a characteristic microbathymetric signature, with spikes and small-scale lumps, that corresponds to the "lumpy" seafloor morphology described previously for the MLSHF (Ondreas et al., 2009) (Figure 2a), and for other hydrothermal fields along mid-ocean ridges (Ferrini et al., 2008; Jamieson et al., 2014) elsewhere (Figure 2b). This lumpy terrain can be clearly differentiated from the volcanic seafloor morphology (hummocks, lava flows, lava channels) that tends to be spatially larger structures (tens to hundreds of m) and that displays instead a smooth seafloor morphology lacking spikes.

Zones with rubble, which are systematically found along slopes of fault scarps or volcanic structures, show instead a granulated texture due to individual rock blocks, which are systematically smaller than hydrothermal structures (~1-2 m or less, Figure 2a). This hydrothermal seafloor texture, which is common to hydrothermal fields (e.g., Lau Basin, Figure 2b) (Ferrini et al., 2008; Jamieson et al., 2014), is used here to map the extent of hydrothermal sites within a hydrothermal field, or of new hydrothermal fields. High-resolution acoustic backscatter, which can reveal this 'lumpy' hydrothermal terrain under optimal insonification conditions, is used to complement the microbathymetry.

Imagery (Figure 1a) is critical to confirm that sites identified in the microbathymetry do correspond to hydrothermal deposits, active or inactive. It is also required to map areas of diffuse hydrothermal outflow, young hydrothermal activity, or fossil structures, with no clear morphological signature (bacterial mats, vents, hydrothermal staining, dead

chimneys, etc.). Extensive seafloor photomosaics are available for the MLSHF, where the hydrothermal activity has been extensively mapped (Barreyre et al., 2012), and additional photomosaics are available for an area ~2 km south of this site, along the ridge axis (Figure 1a). The rest of the imagery is acquired along HOV, ROV, or tow tracks (Figure 1a), which is adequate to identify areas of hydrothermal activity but cannot be used to properly constrain the extent and limits of these areas.

Hence, the areas of 'lumpy' hydrothermal terrain identified in this study, based on microbathymetric data (Figure 1b), indicate zones of significant and sustained hydrothermal activity with significant sulfide accumulation. The bathymetric data also reveal numerous volcanic features (hummocks, volcanic cones), tectonic structures (fault scarps and fissures), and mass wasting indicators (slump scars, debris flows, scree, dejection cones).

Water column studies have also been used to identify hydrothermal activity. High-temperature black smoker type fluids form buoyant plumes in the water column that can be detected from turbidity and manganese anomalies (Klinkhammer et al., 1985; Baker et al., 2001; Baker, 2007; German et al., 2010), while methane anomalies can be associated with sites showing both high-temperature venting (Lupton, 1990) and low-temperature serpentinization (Bougault et al., 1993; Charlou and Donval, 1993; Gràcia et al., 2000). The observations and datasets (microbathymetry, imagery, water column studies) available along the Lucky Strike segment show thus limitations in the ability to detect diffuse and very low-temperature outflow or conductive cooling, that are not associated with either sulfide mounds (Figure 2) or with visual indicators of hydrothermal activity (bacterial mats, anhydrite and other hydrothermal mineral deposits).

3. Hydrothermal sites at the Lucky Strike segment

Based on both the imagery and the microbathymetry shown in Figure 1, we have characterized the distribution and nature of hydrothermal discharge throughout the rift valley floor of the Lucky Strike segment. The distribution of hydrothermal activity and deposits of the Main Lucky Strike hydrothermal field have been mapped in recent studies (Ondréas et al., 2009; Barreyre et al., 2012). Using the new microbathymetric data we have identified additional hydrothermal deposits at the western edge of this main hydrothermal field and extended its limits (Figure 3, Table 1). We also report

three additional hydrothermal sites along the Lucky Strike segment (Figure 3). Two out of these three new sites, Ewan and Capelinhos, have been visited and are confirmed to be active. The third site at the MLSHF has been visited and confirmed to be inactive (H6; Figure 4). The fourth site, Grannus, has been identified solely from the microbathymetric seafloor texture, but lacks direct visual observations to determine if it is active or inactive, or what may be the nature of the associated hydrothermal deposits.

3.1. Main Lucky Strike hydrothermal field (MLSHF)

The MLSHF has been systematically mapped and studied during the last two decades since its discovery in the 90's (Supplementary Table 1) (Langmuir et al., 1997; Humphris et al., 2002; Escartín et al., 2008; Ondréas et al., 2009; Barreyre et al., 2012; Barreyre et al., 2014b; Mittelstaedt et al., 2012). Microbathymetry acquired during the Momareto'06 survey has been used to identify the extent, nature, and limits of several areas corresponding to hydrothermal deposits and associated debris (1 though 4 in Figure 3, Table 1). This morphological mapping is complemented by large-area seafloor photomosaics (Escartin et al., 2008; Barreyre et al., 2012; Mittelstaedt et al., 2012; Prados et al., 2012), used to determine the distribution of both fossil and active venting (Barreyre et al., 2012) both within these hydrothermal areas and elsewhere throughout the field (Figure 3).

The data collected during the MOMAR'08 and Bathyluck'09 cruises reveal two new hydrothermal areas at the MLSHF (Areas 5 and 6 in Figure 3). Area 5, which is located in the southwestern part of the MLSHF and within the axial graben (Figure 3, Table 1), is associated with zones of diffuse flow and scattered active and inactive vents that are visible in the microbathymetry.

Area 6 is located ~1.5 km from the center axis at the western edge of the MLSHF, and in the immediate vicinity of the main fault scarp bounding the axial graben. The seafloor in this area, which corresponds to the flank of an axial volcano recently rifted, is cross-cut by small-scale normal faults with vertical displacements of up to a few meters, and with 'lumpy' hydrothermal seafloor texture (Figures 3, 4). Area 6a corresponds to a broad mound with several spikes (vents) extending over an area of ~70x70 m (Figure 4), and that buries a normal fault scarp that is visible towards the North. Areas 6b and 6c, which had been previously identified in microbathymetric data (Ondréas et al., 2009), are smaller and show instead several isolated spikes and no clear mound. Observations from

VICTOR#605 dive (MOMARSAT'15 cruise, Figure 4) found no evidence of active hydrothermal activity, but confirmed that the pinnacles correspond to fossil hydrothermal chimneys (Figure 4c), and that the area displays numerous indicators of fossil hydrothermal outflow such as smaller hydrothermal mounds (Figure 4d), hydrothermal staining, sulfide rubble, shell chaff, and hydrothermal slab similar to that found at the center of the MLSHF.

3.2. Ewan

The Ewan hydrothermal field was serendipitously discovered during HOV Nautile dive 1624 (Graviluck 2006 cruise, Supplementary Table 1). This dive crossed a series of seafloor patches covered with filamentous bacterial mats that are white and highly reflective when illuminated, associated with mussel beds, and primarily found along scarps and slopes covered with rubble and sediment (Figure 5a-c). Following its discovery, the site was fully surveyed to obtain seafloor photomosaics and microbathymetry (Figures 5d-g, MOMAR'08 and Bathyluck'09 cruises, Supplementary Table 1, Supplementary data). Ewan is located within the axial graben dissecting the central volcanic cone (Escartín et al., 2014), ~2 km south of the MLSHF (Figures 3 and 5f). The seafloor here displays a complex set of horst and graben (Figure 5f), with numerous east- and west-verging normal faults that confine the most recent, unsedimented lava flows (Escartín et al., 2014).

In the photomosaics bacterial mats correspond to white areas with a mottled seafloor aspect (Figures 5c-d), with irregular and gradational limits. Owing to the resolution of the photomosaics (5-10 mm per pixel), we can also identify macrofauna associated with the vents (e.g., fish, Figure 5e), but mussel beds associated with the bacterial mats are not visible in this imagery. Using mapping techniques and interpretation developed earlier (Barreyre et al., 2012), we identified and digitized ~150 larger patches, in addition to >400 that are too small to be digitized, and for which we only record their position. The ~150 digitized patches cover ~275 m^2, whilde the rest correspond to ~30 m^2, attributing 0.06 m^2 to each of the smaller features (~0.25x0.25 m^2). These estimates (Table 2) are likely minima as topography is not accounted for (flat projection), and the photomosaic have gaps where active areas may occur.

Ewan contains several clusters of bacterial mats along a NNE-SSW direction, extending ~250 m along-axis and ~40 m across axis, and in the continuation of aligned pits ~10 m deep and ~30 m wide (Figure 4g). Bacterial mats occur both along slopes (pits, fault scarps, Figure 5a-c) and flat-lying, volcanic seafloor (ropy lavas, RL, in Figure 5d).

294 Detailed HOV observations (Figure 3c) revealed shimmering locally, as observed in
295 diffuse outflow areas at the MLSHF. We did not find active nor fossil high-temperature
296 venting (e.g., active or fallen chimneys) during the HOV dive or in the seafloor
297 photomosaics, suggesting that Ewan hosts only diffuse hydrothermal activity. The
298 distribution and shape of individual bacterial patches also indicates fluid percolation
299 through the seafloor at very slow flow rates.

300

301 *3.3. Capelhinhos*

302 Capelinhos is a vent field located ~1.5 km E of the MLSHF, on the western, outward-
303 dipping flank of a summital volcanic cone (Figures 3 and 6) first identified in the
304 microbathymetric data (Bathyluck'09 cruise). The site was first visited during an ROV
305 dive in 2013 (MoMARSAT'13 cruise, Supplementary Table 1), which confirmed its
306 activity. The microbathymetry shows a main hydrothermal mound that peaks ~20 m
307 above the surrounding seafloor, centered along the trace of a small fault scarp and
308 fissure now buried by the hydrothermal deposits (Figure 6d). This hydrothermal edifice,
309 which links with nearby structures that rise a few meters to 10 m above surrounding
310 seafloor (Figure 6d), shows a low acoustic backscatter and lacks any clear texture in the
311 sonar imagery (Figure 6e). ROV dives (Figure 6d) have confirmed the presence of both
312 inactive and active chimneys with high-temperature outflow through black smokers,
313 clear vents, and flanges (Figure 6a-c). Visual observations suggest that diffuse flow is
314 limited at this site, but we lack seafloor photomosaics to accurately evaluate the type,
315 geometry, and distribution of diffuse flow as done for Ewan and the MLSHF.

316 At a distance of 150 m to the southwest of the Capelinhos vent the bathymetry shows a
317 ~50 m diameter dome rising ~2-3 m above surrounding seafloor, which has not been
318 visited to date (Figure 6d). Nearby fissures immediately to the north expose layered
319 deposits, reminiscent of hyaloclastite layers blanketing the MLSHF (Ondreas et al., 1997;
320 Ondreas et al., 2009). This structure is located in the immediate vicinity of the fault
321 buried by Capelinhos, and its associated acoustic backscatter is low and the sonar
322 featureless, as observed for the main vent structure (Figure 6e). A hydrothermal origin
323 is inconsistent with its surface morphology, which lacks the typical 'spikes' found in
324 hydrothermal terrain. Irregular terrain found East of Capelinhos is instead of volcanic
325 origin (Figures 6d and e). ROV observations in the area show a sedimented seafloor with
326 pillows visible locally, with no evidence of standing hydrothermal chimneys of mounds,
327 and possible hydrothermal staining that is local and minor, and that has not been

sampled. The associated sonar imagery shows a hummocky volcanic texture that is common along the axial seafloor of the Mid-Atlantic Ridge (Smith and Cann, 1990; Yeo et al., 2011).

3.4. Grunnus

Microbathymetric data and sonar imagery show a possible off-axis hydrothermal field, named Grunnus (Figure 7), ~2.5 km west of the MLSHF and corresponding to a spreading age of ~220 kyrs (Table 1). This structure has a diameter of ~200 m, with steep flanks, and a platform ~40-50 m above the surrounding seafloor to the S, and that abuts against the coalescing volcanic cones and hummocks on the flanks of the rifted central volcano to the north. This platform hosts a 20-m high structure that casts a clear shadow in the sonar imagery towards the E (Figure 7b). The shape and size of Grunnus is reminiscent of that of the TAG hydrothermal mound, which ha a pancake shape ~200 m in diameter and ~50 m in height (Humphris and Kleinrock, 1996). Microbathymetry and the sonar data show by small-scale rugosity and pinnacles at its surface that we attribute to hydrothermal structures (chimneys, mounds). The volcanic mounds to the north display instead a smooth surface (Figure 7).

While the mound at Grunnus has not been visited, we suggest that this off-axis site is likely inactive. Observations during an HOV dive conducted in 2006 (Graviluck'06 cruise, Figure 7a) that approached the base of Grunnus yielded no evidence of hydrothermal deposits, activity, nor indicators of present or past fluid flow. Furthermore, water column studies nearby (Wilson et al., 1996; Thurnherr et al., 2008) lack a hydrothermal plume signature, and seismic reflection and refraction data (Singh et al., 2006; Crawford et al., 2010; Combier et al., 2015) do not image an underlying AMC that may act as a heat source for an active hydrothermal field.

Bathymetry and sonar imagery also show a fault cross-cutting the western flank of the mound. The fault scarp is well defined and sharp towards the southwest of the mound, where it shows up to ~5 m of vertical throw and crosscuts seafloor lacking hydrothermal texture. Across the mound this fault scarp is recognizable but is not as well-defined, suggesting that deformation postdated mound emplacement and growth. The difference in fault morphology and height between the mound and surrounding seafloor may be attributed to the different mode of faulting in poorly consolidated hydrothermal deposits relative to basaltic seafloor.

4. Discussion

4.1 Magmatic controls on distribution of hydrothermal activity

The review and analysis of seafloor imagery and microbathymetric data along the Lucky Strike segment (Figure 1) has allowed us to map new areas with fossil hydrothermal deposits at the western edge of the MLSHF. The location of the four sites at the segment center, and the lack of any visual or bathymetric indicators of hydrothermal activity elsewhere along the segment, suggest a link between melt focusing to the segment center and heat sources stable over long periods of time generating hydrothermal activity. Our results do not preclude hydrothermal activity elsewhere, that would be undetected in the absence of visual imagery (diffuse venting with no morphologic signature), in areas imaged but lacking detailed observations to detect low-temperature flow that is not associated with bacterial mats or anhydrite deposits, or in areas where no near-bottom data exists (see section 4.4. for discussion of water column studies).

Of the three active fields, MLSHF and Ewan are at the summit of the central volcano, along the axial graben dissecting it (Ondréas et al., 2009; Escartín et al., 2014), and immediately above the ~3-3.5 km deep axial magma chamber (AMC) (Singh et al., 2006; Combier et al., 2015). The AMC is not centered at the present-day ridge axis, and both Ewan and MLSHF are located towards its eastern edge, while Capelinhos is located ~700 m east of the AMC's edge (Figure 3 and 8). The AMC also extends ~6 km along-axis, likely imparting a three-dimensional thermal structure where temperature gradients can focus flow towards the segment center (Fontaine et al., 2011).

The off-axis Grunnus field is on a volcano flank originally emplaced at the Lucky Strike segment center and since rifted. The original setting is thus similar active on- and near-axis fields along this segment (MLSHF, Ewan, and Capelinhos, Figure 3). It is likely that, as in the case of the hydrothermally active segment center, the Grunnus field may have been animated by a magma chamber underlying the rifted central volcano at the time of its formation, both now extinct.

392 *4.2 Faulting, permeability structure, and outflow at the seafloor*

393 Figure 8 presents a schema of fluid flow within the upper crust associated with the
394 active hydrothermal fields at the active Lucky Strike hydrothermal field, based on
395 geological observations and geophysical data. First, the permeability of the crust
396 immediately above the AMC is likely lower than that of the shallow crust Layer 2A
397 (Barreyre et al., 2014a) owing to its composition and the confining pressure (Figure 8).
398 This crustal section must host the hydrothermal upwelling animated by the presence of
399 the AMC, likely to be distributed and in the form of broad hydrothermal plumes of up to
400 1 km in diameter for reasonable crustal permeabilities (Fontaine et al., 2014), as shown
401 in Figure 8.

402 Second, fluid flow at the seafloor is not broadly distributed, but localized along or near
403 faults. This has been well documented for individual vents and areas of diffuse flow
404 within the MLSHF through detailed hydrothermal and tectonic mapping (Barreyre et al.,
405 2012), and for the newly discovered active sites. Ewan is set on tectonic depressions
406 within the axial graben (Figure 5), while the Capelinhos edifice and associated
407 structures are set at the continuation of fault traces visible in surrounding seafloor
408 (Figure 6), covered subsequently by hydrothermal deposits. This association between
409 hydrothermal outflow and faults, widely observed at other deep-sea hydrothermal fields
410 at all spreading ridges and in different tectonic environments (Kleinrock et al., 1993;
411 Haymon et al., 2005; Pedersen et al., 2010; Marcon et al., 2013), suggests that permeable
412 faults channel hydrothermal flow in the shallow crust (Barreyre et al., 2012; Barreyre et
413 al., 2014a), as illustrated in Figure 8.

414 Rifting and diking at the Lucky Strike segment center have concentrated along the ~1
415 km-wide axial graben dissecting the Lucky Strike central volcano (Humphris et al., 2002;
416 Ondréas et al., 2009; Escartín et al., 2014). These processes may play an important role
417 in the permeability of the crust overlying the AMC, with the development of a zone of
418 high-permeability following the axial graben, and induced by thermal cracking and
419 fracturing associated with dike emplacement, and by small-scale faulting that is likely
420 limited to the shallowest 1-2 km of the crust (Figure 8). An anisotropic permeability
421 structure, coupled with a magma chamber, can promote along-axis convection cells
422 (Fontaine et al., 2014) consistent with microseismicity clusters observed here above the
423 AMC (Crawford et al., 2013), with clusters resulting from cracking-induced
424 microseismicity induced by cooling. It is thus likely that the two microseismicity clusters
425 along the axial graben, one immediately north of the MLSHF, and the second below the

summit of the axial volcanic cone (Figure 3) correspond to cooling in downflow areas. Venting at Capelinhos, which is East of the AMC edge, is then likely associated to flow along a permeable fault that may root at the main upwelling zone and below the Layer 2A (Figure 8). Ewan may correspond instead to a minor axial upwelling relative the MLSHF, and associated with a downwelling area below the rifted axial volcano located between these two hydrothermal fields (Figure 3). Alternatively, Ewan may be associated with a recent magmatic event such as the emplacement of a lava flow or dike propagation in the shallow crust as suggested by hydrophone data (Dziak et al., 2004).

4.3 Revised hydrothermal heat flux at Lucky Strike

The new observations and results presented here allow us to update the heat flux estimates of known hydrothermal activity at the Lucky Strike segment (Ewan and Capelinhos in addition to MLSHF), based on visual and instrumental observations. A prior estimate of heatflux for MLSHF, based on the photomosaic and a systematic evaluation of the distribution of vents, yielded values of 195-1086 MW (Barreyre et al., 2012). As the only new hydrothermal area within this field found in this study is inactive, this estimate remains unchanged.

Ewan displays only diffuse and low-temperature hydrothermal discharge, that we have fully mapped using the seafloor photomosaics (Figure 5). Adopting the methodology of Barreyre et al. (2012), we estimate the minimum and maximum heatflux based on the area of diffuse outflow estimated from the photomosaics (Figure 3), and the estimated temperature and velocity of the outflow from studies in similar settings (see details in Barreyre et al., 2012, and Table 2). We obtain a heatflux estimate that ranges from 4.4-117 MW. In our calculations we likely underestimate the surface of diffuse outflow, as it is calculated over images projected to a horizontal plane without taking into account the steep topography present in the area (Figure 5). As in the case of the MLSHF diffuse fluxes, other uncertainties are the velocity and the temperature of the diffuse outflow, which are not constrained by systematic measurements at this site. Visual inspection of the Capelinhos site shows that there are two active main chimneys with a total of ~10-15 vents identified (Figure 4), in addition to flanges with diffusers. Assuming a total of 10-20 vents with a heatflux of 0.12-0.8 MW/vent (Barreyre et al., 2012; Mittelstaedt et al., 2012) we estimate the Capelinhos heat-flux at 1.2-16 MW.

The hydrothermal heat flux that we estimate for the new active sites (5.6-133 MW, Table 2) are thus minor relative to the 195/1086 MW previously reported for the MLSHF (Barreyre et al., 2012). This represents an increase of ~10% in our heatflux estimate

460 that is taken up primarily by diffuse hydrothermal outflow (80-90% of the total heatflux,
461 Table 2), although the importance of diffuse outflow appears to vary greatly from site to
462 site (100% at Ewan and almost non-existent at Capelinhos).

463 *4.4 Water column anomalies and elusive hydrothermal plumes*

464 Water column studies throughout the Lucky Strike segment report anomalies attributed
465 to hydrothermal plumes rising from undiscovered fields, although their. evidence is
466 elusive. Light transmission anomalies and elevated CH_4 concentrations south of the
467 MLSHF and central volcano (Wilson et al., 1996) have been attributed to an unidentified
468 but large field at ~2100 m (W in Figure 9). During the HEAT cruise (German et al.,
469 1996), TOBI deep-tow sonar detected one anomaly along the non-transform offset
470 between Lucky Strike North and Famous segments, and another one at the southern
471 edge of the nodal basin during a hydrographic cast (G in Figure 9). More recently,
472 hydrographic stations revealed a water column anomaly at 1800 m bsl at the southern
473 segment end (Thurnherr et al., 2008) (T in Figure 9). Finally, CH_4 anomalies indicating
474 low-temperature hydrothermal activity associated with serpentinization and not linked
475 to black smoker activity (lack of a manganese signature) have been identified at Menez
476 Hom (Gràcia et al., 2000), and at the southern inside-corner of the Lucky Strike segment
477 (Gr in Figure 9).

478 Numerous other hydrographic profiles conducted throughout this segment show no
479 water column anomaly. These including casts during the Graviluck cruise shown in
480 Figure 9 (Thurnherr et al., 2008), ROV dives during the cruises in 2008 and 2009 (Figure
481 9 and Supplementary Table 1), or deep-towed surveys using TOBI (German et al., 1996;
482 Gràcia et al., 1998), which detected no water column anomalies other than those along
483 the non-transform offset and the end of the segment (German et al., 1996) (Figure 9). In
484 many casts, the plume of the MLSHF is not detected (Figure 9), likely due to complex
485 hydrography and strong seafloor currents (Thurnherr et al., 2008) that may sweep or
486 dilute its plume. Furthermore, seafloor observations and microbathymetry surveys
487 available in the immediate proximity of some of these anomalies (Figure 9) provide no
488 evidence of activity away from the three active hydrothermal fields at the center of the
489 segment (Figure 3). Therefore the evidence for additional undiscovered hydrothermal
490 fields inferred along the southern portion of the Lucky Strike segment (Wilson et al.,
491 1996; German et al., 1996; Thurnherr et al., 2008) is weak owing to the unexplained
492 spatial and temporal inconsistencies of hydrographic data indicating the presence or
493 absence of hydrothermal plumes, the lack of visual or morphologic indicators of

hydrothermal activity away from the segment center, and the complex hydrography of the area.

4.5. Significance for hydrothermal activity along slow spreading segments

Central volcanoes other than Lucky Strike host active vents. At intermediate-spreading ridges, Axial Volcano along the Juan de Fuca Ridge is also underlain by a magma chamber 2.5-3.5 km below seafloor, hosts several hydrothermal sites that are monitored (Kelley et al., 2014). At slower-spreading ridges, the Menez Gwen field (Ondreas et al., 1997; Marcon et al., 2013) and the Kobeinsey field (Olafsson et al., 1989) along the Mid-Atlantic Ridge, and the Soria Moria and Troll Wall along the Arctic Ridges (Pedersen et al., 2010) all occur on central volcanoes at similar phases of rifting as that of Lucky Strike, dissected at the summit by narrow and localized axial graben. It is likely that these sites are also underlain by magma chambers linked to central volcano formation, and such fields may be common at central volcanoes along ridge segments (Escartín et al., 2014) that are yet unexplored.

Hydrothermal activity at central volcanoes is likely to be persistent over long periods of time, continuously or intermittently, owing to sustained and enhanced melt supply required for their formation. This is supported by the presence of both isolated hydrothermal vents and areas of hydrothermal deposits that are inactive at Lucky Strike (Area 5, Table 1), and by the off-axis Grunnus site on a rifted central volcano. While there are no age constraints on hydrothermal deposits at the Main Lucky Strike hydrothermal field (Figure 3), it likely to have been active over thousands to a few tens of thousands of years (Humphris et al., 2002; Barreyre et al., 2012). Other basalt-hosted hydrothermal fields found along axial volcanic ridges (e.g., Broken Spur (Murton et al., 1994; Murton et al., 1999), Snake Pit (Karson and Brown, 1988), BeeBee (Connelly et al., 2012) or Lilliput (Haase et al., 2009)) are much smaller in size and probably with shorter life-spans. These may be likely associated to short-lived heat sources (e.g., dike intrusions or recent volcanic erutions). The long-lived hydrothermal fields associated with central volcanoes are likely to play a major role in the dispersion and propagation along the ridge-axis of hydrothermal ecosystems and on the biogeography of these communities (Van Dover et al., 2002).

Conclusions

Extensive seafloor imagery and visual observations together with microbathymetry acquired with deep-sea vehicles have allowed us to evaluate the distribution of

hydrothermal activity at the scale of the Lucky Strike segment, and to re-evaluate the associated heatflux. The Lucky Strike segment hosts three active hydrothermal fields: The known MLSHF, Capelinhos, and Ewan. Capelinhos is located 1.3 km E of the axis and the Main field, and consists of a ~20 m sulfide mound with black smoker vents. Ewan is located ~1.8 km south from the Main LS field long the axial graben, and displays only diffuse flow along and around scarps of collapse structures associated with fault scarps. At the Main Lucky Strike hydrothermal field we have identified an inactive site, thus broadening the extent of this field. Heat flux estimates from these new sites are relatively low and correspond to ~10% of the heat flux estimated for the Main field, with an integrated heatflux of 200-1200 MW. Overall, most of the flux (up to 80-90%) is associated with diffuse flow, with the Ewan site showing solely diffuse flow and Capelinhos mosty focused flow. The microbathymetry also reveals a large, off-axis (~2.4 km) hydrothermal field, comparable to the TAG mound in size, on the flanks of a rifted volcano. The association of these fields to a central volcano, and the absence of indicators of hydrothermal activity along the ridge segment, suggest that sustained hydrothermal activity is maintained by the enhanced melt supply and the associated magma chamber(s) required to build central volcanoes. In all cases hydrothermal outflow at the seafloor is controlled by faults, indicating that these tectonic structures are permeable and exploited by the hydrothermal circulation in the shallow crust. Our observations, together with inconsistencies in available oceanographic data, also fail to constrain the possible source(s) of all anomalies detected in water column. Central volcanoes are thus associated with long-lived hydrothermal activity, and these sites may play a major role in the distribution and biogeography of vent communities.

Acknowledgements. This work has been partly financed by ANR (France) Mothseim Project NT05-3 42213 to JE, by EU-RTN-MOMARNET to MC, and by MINECO (Spain) project CTM2013-46718-R to RG. The French Ministry of Research financed ship, ROV and AUV time (Graviluck'06, MOMAR'08, Bathyluck'09, MOMARSAT cruises in 2010-2015). *TowCam* deployment during Graviluck cruise was supported by NSF grant OCE-0623744 to A. Soule and D. J. Fornari (WHOI, USA). This is IPGP contribution #3676.

Table 1. Hydrothermal fields at the Lucky Strike ridge segment. The limit of sites H1 through H4 in the Main Lucky Strike field have been defined previously (Ondréas et al., 2009), as well the distribution of focused and diffuse hydrothermal outflow by (Barreyre et al., 2012). Sites H5 and H6 in the Main Lucky Strike Field, and the Ewan, Capelinhos, and Grunnus fields are described in this paper.

Name	*Longitude*	*Latitude*	*Depth, m*	*Area, m²*	*Distance, km (spreading age, kyr)#*	*In situ data*	*Activity**
Main Lucky Strike field					0-0.6 (0-53)	Visual, photomosaic	
H1	32°16.92'W	37°17.61'N	1620-1720	30304			Active, f+d
H2	32°16.50'W	37°17.48'N	1620-1670	35535			Active, f+d
H3-Eiffel Tower	32°16.52'W	37°17.33'N	1680	1506			Active, f+d
H3a	32°16.60'W	37°17.43'N	1670	5066			Active, f+d
H3b	32°16.62'W	37°17.37'N	1680-1700	3856			Active, f+d
H3c	32°16.52'W	37°17.27'N	1700	1454			Active, f+d
H4	32°16.90'W	37°17.41'N	1710	282			Active, f+d
H5	32°16.84'W	37°17.39'N	1725	10429			Active, f+d
H6a	32°17.08'W	37°17.71'N	1585	4479			Inactive
H6b	32°17.05'W	37°17.64'N	1590	2259			Inactive
H6c	32°17.07'W	37°17.69'N	1590	2597			Inactive
Ewan	32°17.27'W	37°16.61'N	1770	3010	0 (0)	Visual, photomosaic	Active, d
Capelinhos	32°15.83'W	37°17.35'N	1665	20712	1.4 (130)	Visual	Active, f (d)
Grunnus	32°18.25'W	37°18.02'N	1645	35704	2.4 (220)	None	Inactive?

Notes: #Distance is measured to centerline of axial graben, and spreading age calculated assuming a full spreading rate of 22 km/Myr. For the main Lucky Strike we report the minimum and maximum distances and the associated spreading ages.

*Activity of sites is confirmed visually except for Grunnus, which has not been visited to date. Type of flow: f - focused flow (vents); d - diffuse flow. Type of flow in parenthesis denotes minor occurrence.

588 **Table 2**. Ranges (min/max)? Heatflux estimates of Lucky Strike hydrothermal fields.
589 Calculations are based on the number of high-temperature vents and surface of areas of
590 diffuse flow identified visually (this ?study) and instrumental measurements (temperature,
591 currents), following the methodology of Barreyre et al. (2012).

592 *Ewan hydrothermal field (diffuse)*

593 Large patches:	S: 274 m^2	Q=4.2/92 MW
594 Small matches:	Number=1072; S: 11 m^2	Q=0.2/15 MW
595 Total EWAN		Q=**4.4/117 MW**

596

597 *Capelinhos hydrothermal field (focused)*

598 Vents	Number= 10-20; Q/vent=0.12-0.8 MW	Q=**1.2/16 MW**

599

600 *Main Lucky Strike hydrothermal field (focused + diffuse)* (Barreyre et al., 2012)

601 Diffuse flow	Q=187/1036 MW
602 Focused flow	Q=8/50 MW
603 Total MLSHF	Q=**195/1086 MW**

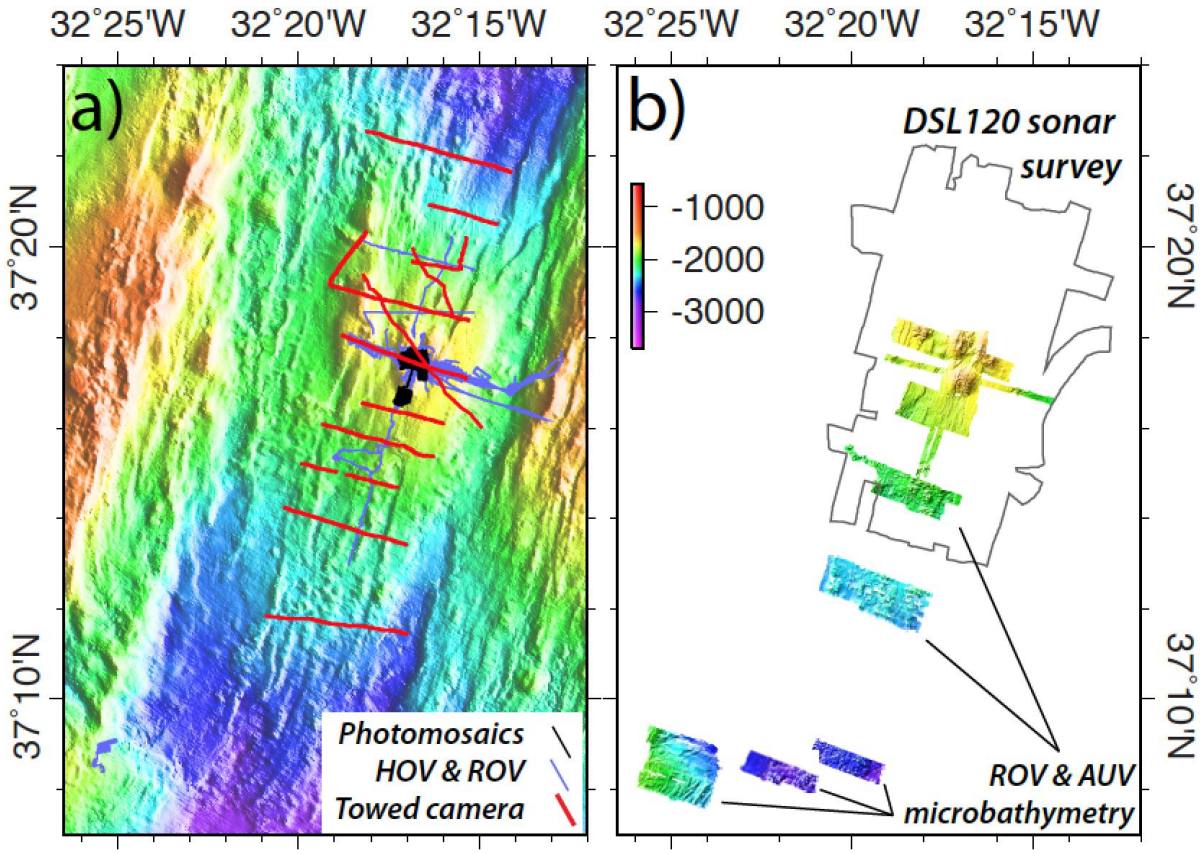
604

605 ***Combined heat-fluxes at Lucky Strike***

606 **Diffuse flow**	**Q=191/1143 MW**
607 **Focused flow**	**Q=9/66 MW**
608 **Total heatflux**	**Q=200/1210 MW**

609 * Diffuse flow: $Q = \Delta T \times \phi \times v \times C_p \times S$, where f is density of seawater (1025 $kg.m^{-3}$), C_p is the
610 specific heat of the diffuse fluid (4.2 10^3 $J.kg^{-1}$ $°C^{-1}$), ΔT is temperature difference T-T_0 between
611 outflow temperature T and ambient seawater T_0 (4.4°C), v is the diffuse effluent velocity, and S
612 the area of considered diffuse outflow (m^2). T minimum and maximum values are 8 and 20°C,
613 and V minimum and maximum values are 1 and 5 mm/s, as described by Barreyre et al. (2012)
614 and references therein. S is reported in the Table 1.

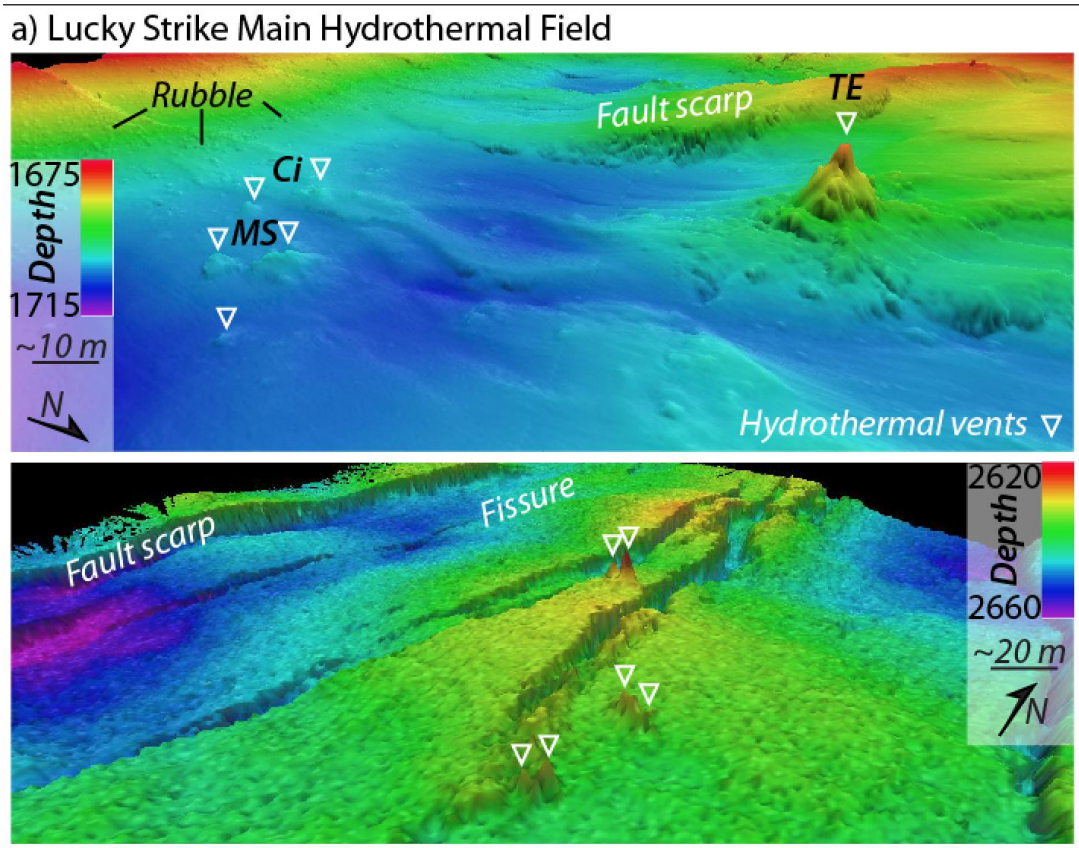
615 Focused flow: Individual vent heatflux is estimated at 0.12-8 MW, as described by Barreyre
616 et al. (2012). The total heatflux associated to focused flow is the integration of the heatflux from
617 individual vents, which are visually identified in available ROV video imagery.



618

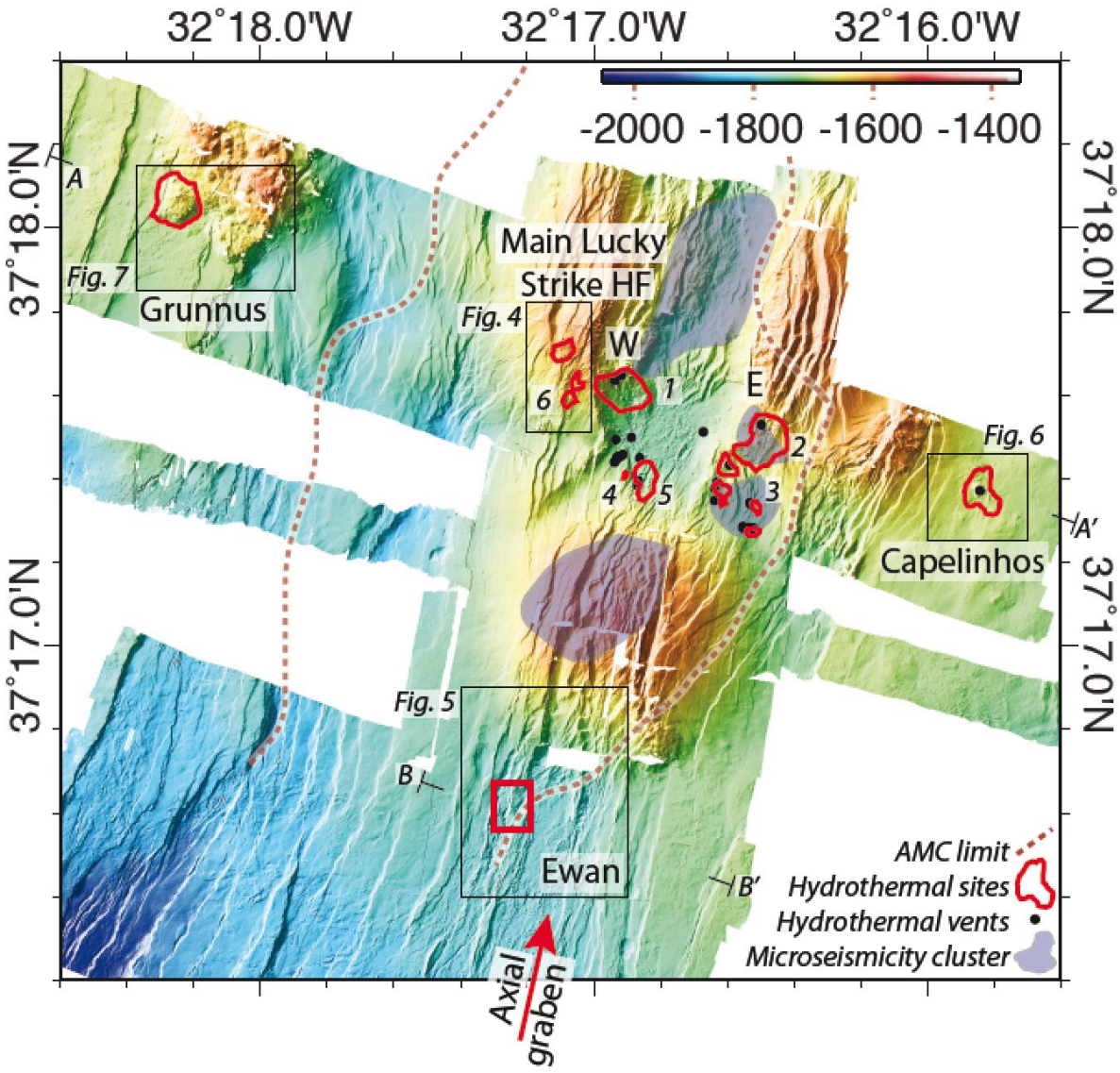
619

620 **Figure 1.** a) Visual information of the seafloor is available from ROV photomosaics, and
621 along tracks of HOVs, ROVs, and deep-towed cameras. b) Available microbathymetric
622 data from the Lucky Strike ridge segment, acquired during near-bottom ROV and AUV
623 surveys (Momareto'06 and MOMAR'08 and Bathyluck'09 cruises). The outline of the
624 DSL120 sonar survey, acquired during the Lustre'96 cruise, is also shown. See
625 Supplementary Table 1 for additional details on these cruises, the deep-sea vehicles
626 deployed, and types of data acquired.



627

628 **Figure 2**. Perspective views showing the 'lumpy' seafloor morphology associated with
629 hydrothermal deposits described in the text. a) Microbathymetry from the Lucky Strike
630 Main Hydrothermal field, showing the ~20 m high Tour Eiffel (TE) vent and the
631 associated hydrothermal deposits around it, and smaller nearby vents (MS: Montsegur;
632 Ci: Cimendef). The view shows also several fault scarps and rubble on slopes, that are
633 morphologically distinct from hydrothermal deposits. b) Microbathymetry showing
634 hydrothermal vents in the Kilo Moana Hydrothermal Field in the Lau Basin (Ferrini et al.,
635 2008; Ferrini and Tivey, 2012), rising ~10-20 m above surrounding seafloor that is
636 faulted and fissured.



637

638 **Figure 3**. Microbathymetry of the Lucky Strike segment center showing the four
639 hydrothermal fields identified and the present-day zone of accretion along the axial
640 graben (red arrow). Red contours correspond to the limits of hydrothermal deposits
641 identified in the microbathymetry, which are numbered for the Main Lucky Strike Field.
642 The red square corresponds to the Ewan field, which lacks a geomorphologic signature,
643 and black dots correspond to active vents. Boxes indicate the location of Figures 4
644 through 7, and characteristics of fields are given in Table 1. The limits of the AMC (Singh
645 et al., 2006; Combier et al., 2015) and location of microseismic clusters (Crawford et al.,
646 2013) are also shown. A-A' and B-B' indicate enpoints of profiles shown in Figure 8a.

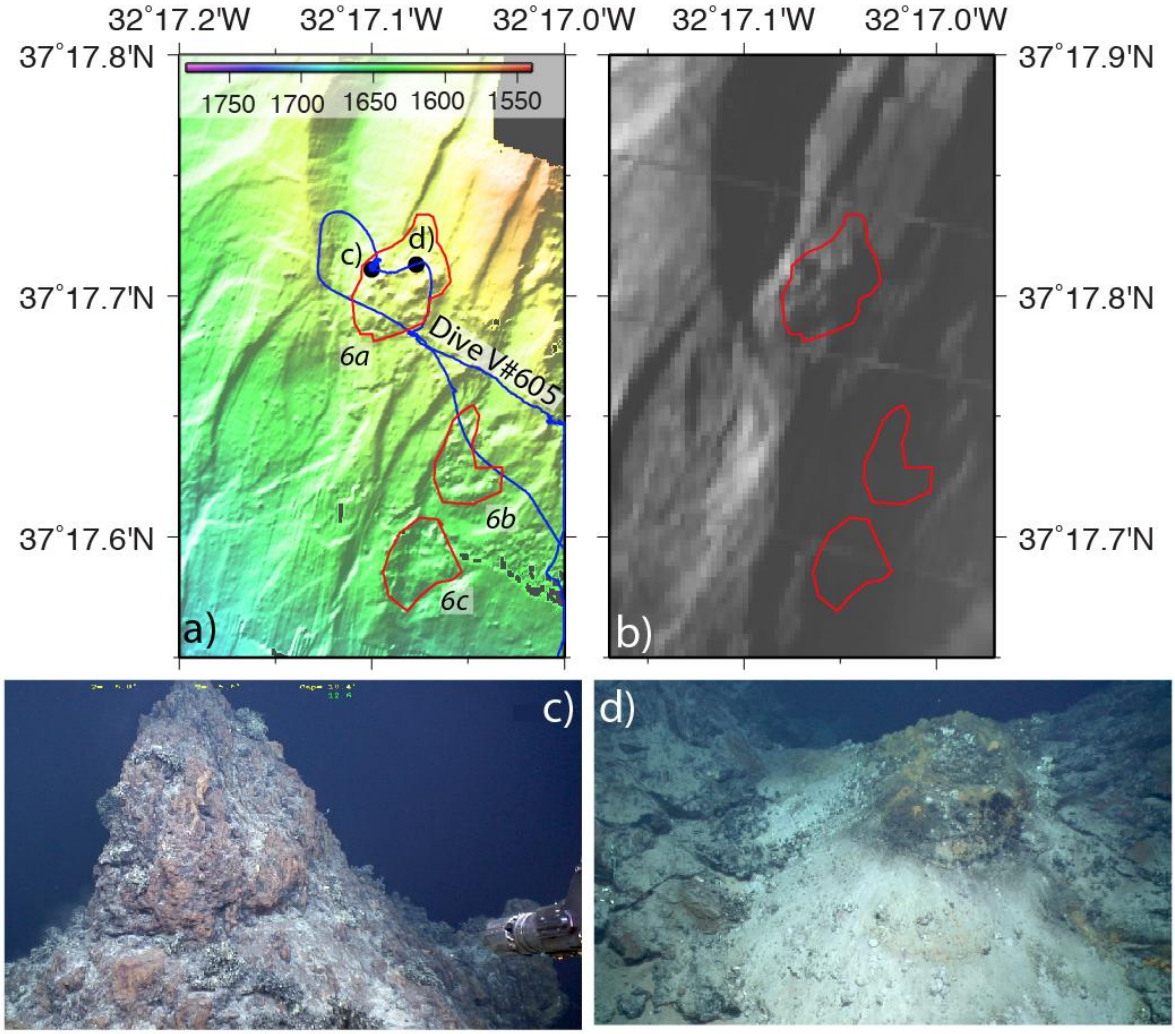


Figure 4. a) Microbathymetry of the western edge of the MLSHF, showing hydrothermal areas 6a-c in red (see Table 1 and Figure 3). c) and d) indicate the location of photos in Figures 4c and 4d, respectively. b) Acoustic backscatter image of the same area, with insonification from the west. Bright areas correspond to high backscatter, and black to acoustic shadows in this and following figures with sonar imagery. c) Inactive chimney and d) hydrothermal mound associated deposits observed during ROV VICTOR dive #605 (blue line).

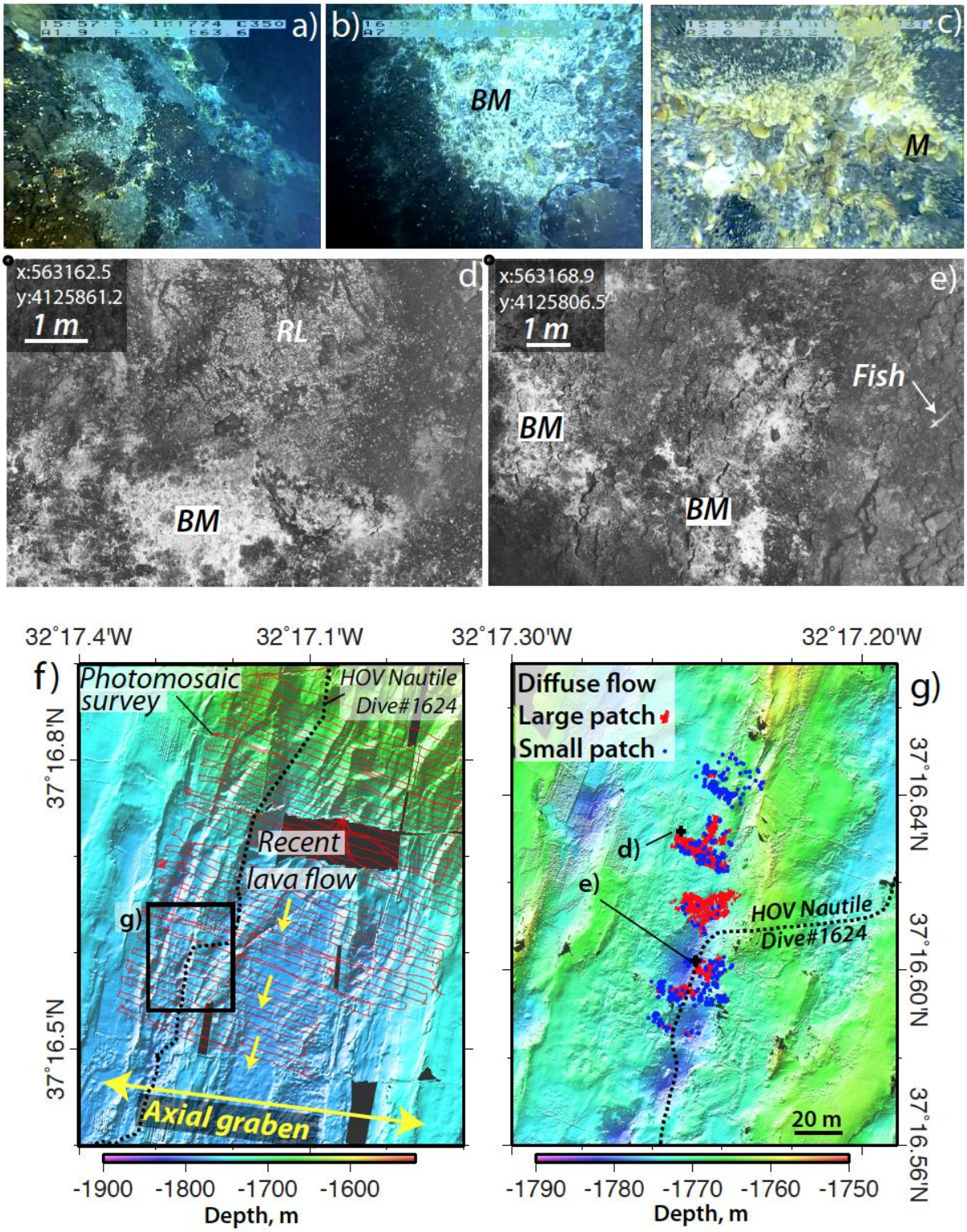


Figure 5. Ewan hydrothermal field. a)-c) Video grabs from HOV Nautile dive #1616 (Graviluck'06) show hydrothermal activity along steep slopes (a), with irregular patches of bacterial mats and diffuse flow through rubble (b), and associated with mussel beds (c). d) Vertical seafloor image mosaics (Bathyluck'09) showing patches of bacterial mats (BM) associated with diffuse flow extending over several meters over sedimented ropy lava flows (RL). e) Irregular bacterial mat patches, indicating localized diffuse outflow through steep scarps. Microbathymetry (50 cm/pixel) of the ridge axis on the southern flank of the rifted seamount south of the Main Lucky Strike field (f) and detail of the active zones (g). The coordinates of the top left corner of the photomosaics d) and e) are in UTM (m), and located in g). See Supplementary Data for photomosaic of this area and digitized zones of hydrothermal outflow.

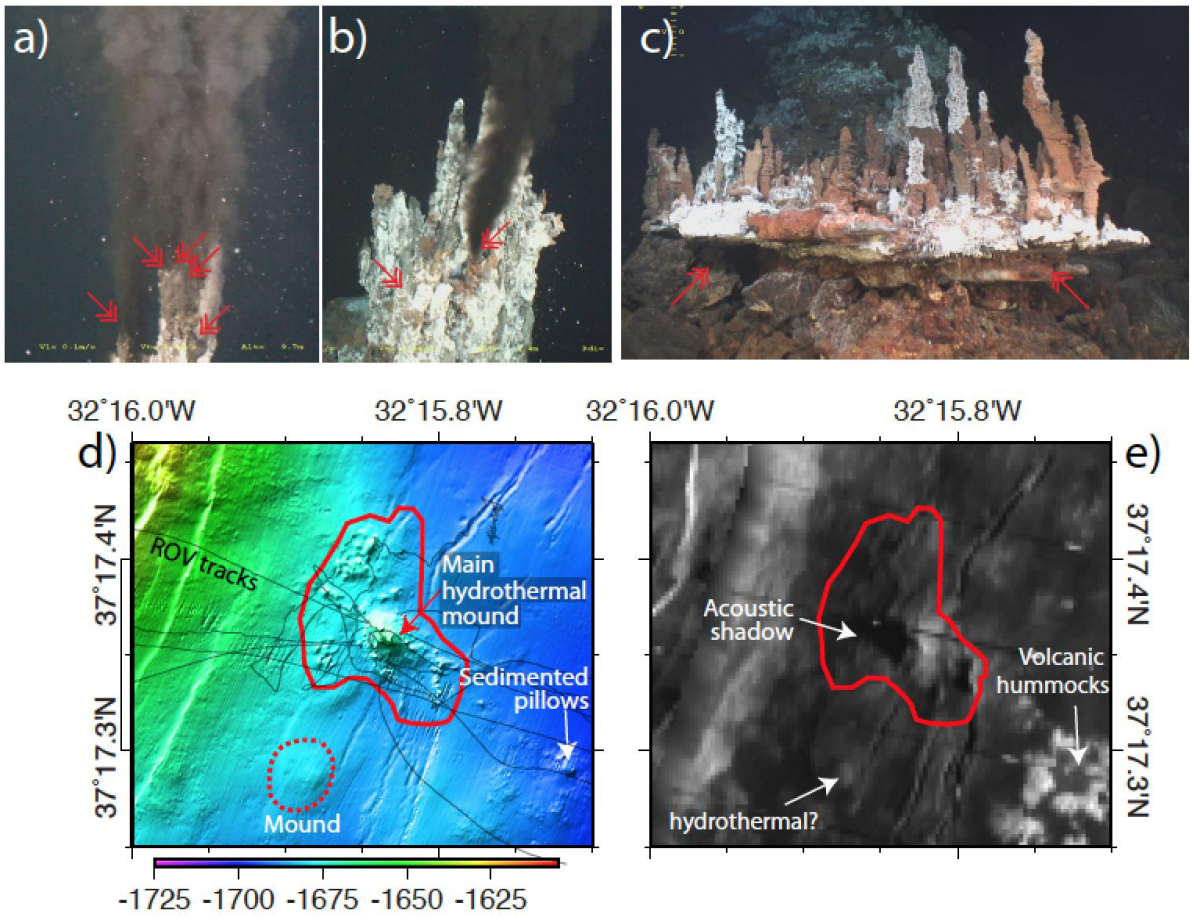
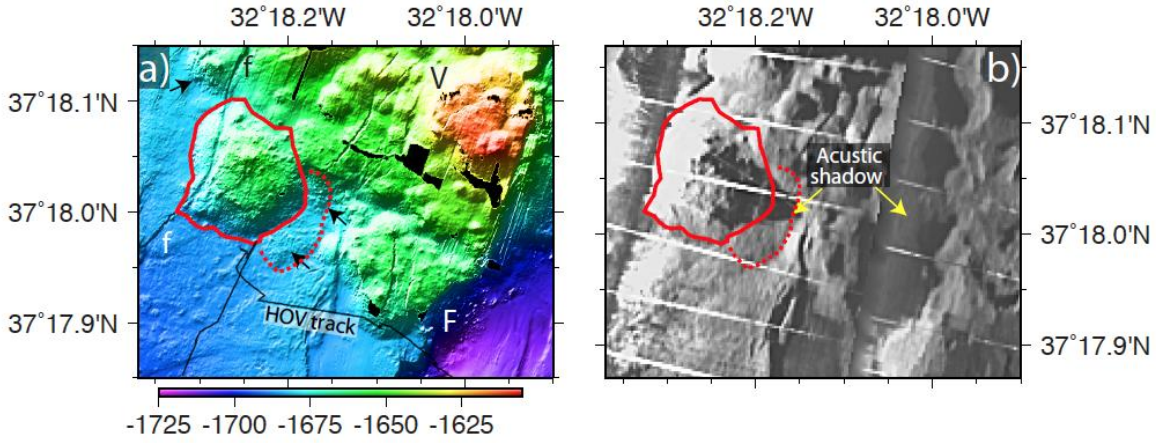


Figure 6. Capelinhos hydrothermal site. The main Capelinhos hydrothermal mound shows active chimneys with several black smoker vents (a-b) flanges with diffusers (c). Diffuse hydrothermal activity (bacterial mats) is scarce. d) Microbathymetry of the Capelinhos hydrothermal field (red outline), which displays a ~20 m high edifice emplaced over a set of small-scale faults and fissures, and a possible hydrothermal mound to the south (not visually inspected). e) Acoustic backscatter image with insonification from the E, showing the acoustic shadow of the edifice. The bathymetry reveals several mounds in surrounding areas (arrows); the structure to the SW has low acoustic backscatter and may correspond to another hydrothermal deposit. The structures to the SE are instead acoustically reflective and the sonar texture corresponds to volcanic hummocks.

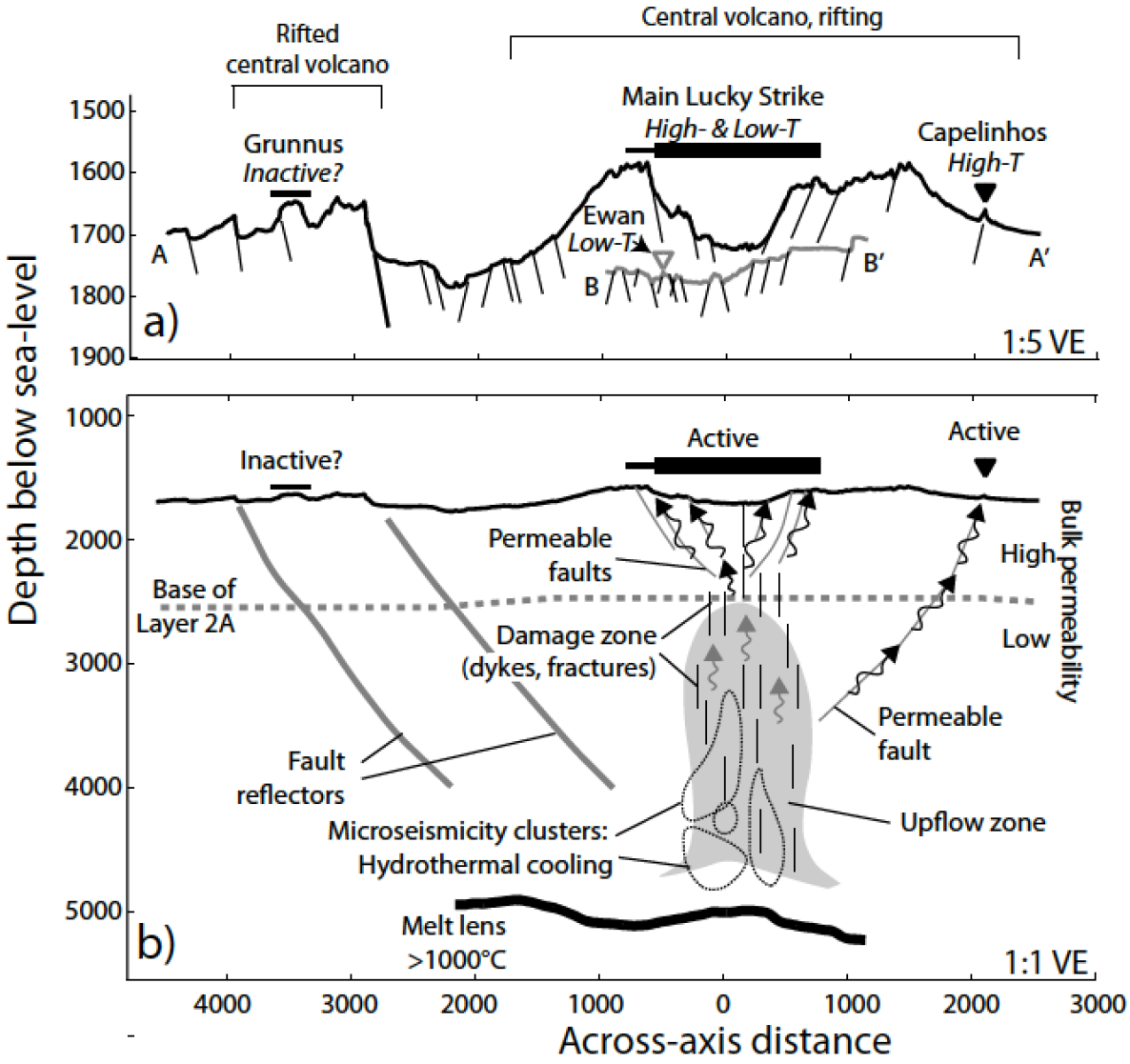


685

686

687 **Figure 7.** a) Microbathymetry of the Grunnus hydrothermal field (solid red line), and
688 other possible hydrothermal structures (black arrows, dashed red line) located on the
689 flank of a rifted central volcano (V, see Figure 3). A small normal fault (f) dissects the
690 western flank of the ~200 meter diameter mound, while major fault (F) that dissects the
691 central volcano can be linked to a fault seismic reflector to a depth of ~2 km below
692 seafloor (Smith et al., 2006; Combier et al., 2015). b) Corresponding sonar imagery of the
693 area.

694



695

696 **Figure 8.** a) Microbathymetric profiles across the Grunnus-MLSHF-Capelinhos (black
697 line) and across Ewan (grey line, see Figure 3 for location). b) Vertical across-axis
698 section of the crust showing the AMC and fault reflectors (Singh et al., 2006; Combier et
699 al., 2015) and the base of Layer 2A (Seher et al., 2010) from seismic data, and the
700 projected positions of microseismicity clusters (Crawford et al., 2013). Hydrothermal
701 upflow below Layer 2A is likely diffuse in the form of upwellings up to ~1 km in
702 diameter (Fontaine et al., 2014) along the axis, which has a higher permeability due to
703 damage induced by diking and cracking (Fontaine et al., 2014; Escartín et al., 2014). In
704 the shallow crust hydrothermal outflow is likely channeled instead along permeable
705 faults.

706

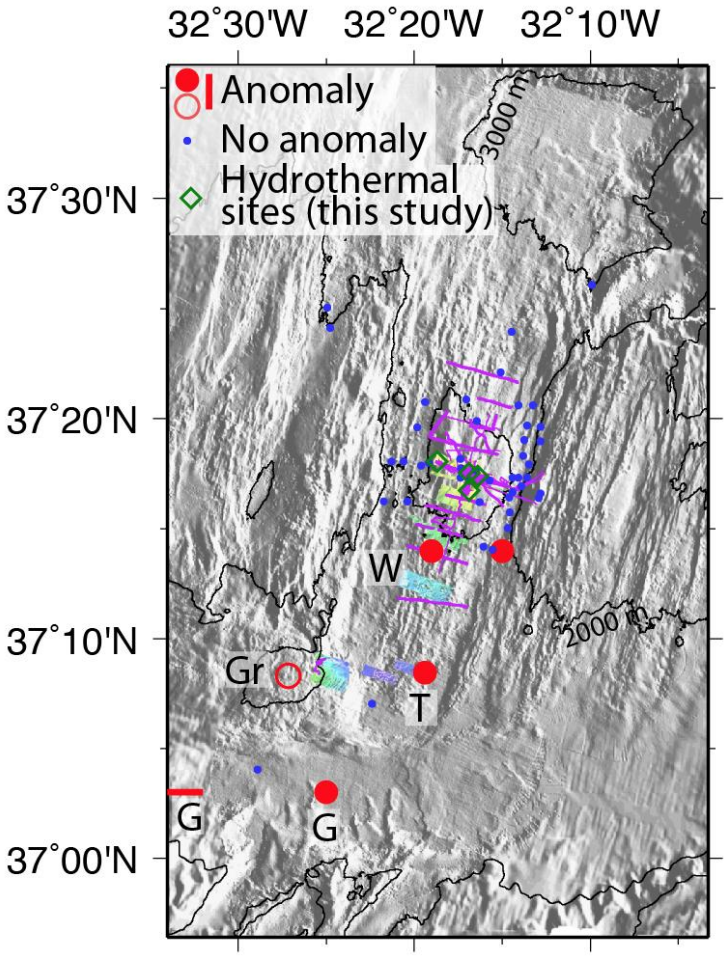


Figure 9. Map of the Lucky Strike field showing the location of water column nephenlometry anomalies interpreted as indicators of hydrothermal plumes at depths of ~1800 m bsl (red), and hydrographic casts conducted during the Graviluck2006 cruise that yielded no anomalies (blue). Shaded relief is from shipboard bathymetry, the purples lines correspond to to visual seafloor observations (Figure 1), the AUV and ROV microbathymetry is shown in color (see Figure 3), and sites described in this paper indicated by green diamonds. Water column anomalies: G: (German et al., 2006); T (Thurnherr et al., 2008); W (Wilson et al., 1996); Gr (Gràcia et al., 2000).

References

Baker, E.T., 2007, Hydrothermal cooling of mid ocean ridge axes: Do measured and modeled heat fluxes agree? Earth and Planetary Science Letters, v. 263, p. 140–150.

Baker, E.T., Cormier, M.-H., Langmuir, C.H., and Zavala, K., 2001, Hydrothermal plumes along segments of contrasting magmatic influence, 15°20'-18°30'N, East Pacific Rise; Influence of axial faulting: Geochemistry, Geophysics, Geosystems, v. 2, p. 2000GC000165.

Barreyre, T., Escartín, J., Garcia, R., Cannat, M., Mittelstaedt, E., and Prados, R., 2012, Structure, temporal evolution, and heat flux estimates from the Lucky Strike deep-sea hydrothermal field derived from seafloor image mosaics: Geochemistry, Geophysics, Geosystems, v. 13, no. 4, p. Q04007, doi: 10.1029/2011GC003990.

Barreyre, T., Escartin, J., Sohn, R., and Cannat, M., 2014a, Permeability of the Lucky Strike deep-sea hydrothermal system: Constraints from the poroelastic response to ocean tidal loading: Earth and Planetary Science Letters, v. 408, p. 146–154, doi: 10.1016/j.epsl.2014.09.049.

Barreyre, T., Escartín, J., Sohn, R.A., Cannat, M., Ballu, V., and Crawford, W.C., 2014b, Temporal variability and tidal modulation of hydrothermal exit-fluid temperatures at the Lucky Strike deep-sea vent field, Mid-Atlantic Ridge: Journal of Geophysical Research: Solid Earth, v. 119, no. 4, p. 2543–2566, doi: 10.1002/2013JB010478.

Bischoff, J.L., and Seyfried, W.E., 1978, Hydrothermal chemistry of seawater from 25° to 350°C: American Journal of Science, v. 278, p. 838–860.

Bougault, H., Charlow, J.-L., Fouquet, Y., Needham, H.D., Vaslet, N., Appriou, P., Jean Baptiste, P., Rona, P.A., Dmitriev, L., and Silantiev, S., 1993, Fast and slow-spreading ridges: Structure and hydrothermal activity, ultramaphic topographic highs, and CH4 output: Journal of Geophysical Research, v. 98, no. B6, p. 9643–9651.

Charlou, J.-L., and Donval, J.-P., 1993, Hydrothermal methane venting between 12°N and 26°N along the Mid-Atlantic ridge: Journal of Geophysical Research, v. 98, no. B6, p. 9625–9642.

Colaço, A., Blandin, J., Cannat, M., Carval, T., Chavagnac, V., Connelly, D., Fabian, M., Ghiron, S., Goslin, J., Miranda, J.M., Reverdin, G., Sarrazin, J., Waldmann, C., and Sarradin, P.-M., 2011, MoMAR-D: a technological challenge to monitor the dynamics of the Lucky Strike vent ecosystem: ICES Journal of Marine Science, v. 68, no. 2, p. 416–424. doi:10.1093/icesjms/fsq075.

Combier, V., Seher, T., Singh, S.C., Crawford, W.C., Cannat, M., Escartín, J., and Dusunur, D., 2015, Three-dimensional geometry of axial magma chamber roof and faults at Lucky Strike volcano on the Mid-Atlantic Ridge: Journal of Geophysical Research: Solid Earth, p. n/a–n/a, doi: 10.1002/2015JB012365.

Connelly, D.P., Copley, J.T., Murton, B.J., Stansfield, K., Tyler, P. a, German, C.R., Van Dover, C.L., Amon, D., Furlong, M., Grindlay, N., Hayman, N., Hühnerbach, V., Judge, M., Le Bas, T., et al., 2012, Hydrothermal vent fields and chemosynthetic biota on the world's deepest seafloor spreading centre.: Nature communications, v. 3, p. 620, doi: 10.1038/ncomms1636.

758 Crawford, W.C., Rai, A., Singh, S.C., Cannat, M., Escartín, J., Wang, H., Daniel, R., and
759 Combier, V., 2013, Hydrothermal seismicity beneath the summit of Lucky Strike
760 volcano, Mid-Atlantic Ridge: Earth and Planetary Science Letters, v. 373, p. 118–
761 128.

762 Crawford, W.C., Singh, S.C., Seher, T., Combier, V., Dusunur, D., Cannat, M., Rona, P.,
763 Devey, C.W., Dyment, J., and Murton, B., 2010, Crustal structure, magma chamber
764 and faulting beneath the Lucky Strike hydrothermal fields, *in* Diversity of
765 Hydrothermal Sytems on Slow Spreading Ocean Ridges, AGU, Washington DC, p.
766 113–132.

767 Van Dover, C.L., German, C.R., Speer, K.G., Parson, L.M., and Vrijenhoek, R.C., 2002,
768 Evolution and Biogeography of Deep-Sea Vent and Seep Invertebrates: Science, v.
769 295, p. 1253–1257.

770 Dziak, R.P., Smith, D.K., Bohnenstiehl, D.R., Fox, C.G., Desbruyères, D., Matsumoto, H.,
771 Tolstoy, M., and Fornari, D.J., 2004, Evidence of a recent magma dike intrusion at the
772 slow spreading Lucky Strike segment, Mid-Atlantic Ridge: Journal of Geophysical
773 Research, v. 109, p. B12102, doi: 10.1029/2004JB003141.

774 Escartín, J., García, R., Delaunoy, O., Ferrer, J., Gracias, N., Elibol, A., Cufi, X., Fornari, D.J.,
775 Humphris, S.E., and Renard, J., 2008, Globally-aligned photo mosaic of the Lucky
776 Strike hydrothermal Vent Field (Mid-Atlantic Ridge, 37°18.5'N): release of geo-
777 referenced data, mosaic construction and viewing software: Geochemistry,
778 Geophysics, Geosystems, v. 9, no. 12, p. Q12009, doi:10.1029/2008GC002204.

779 Escartin, J., Garcia, R., Delaunoy, O., Ferrer, J., Gracias, N., Elibol, A., Cufi, X., Neumann, L.,
780 Fornari, D.J., Humphris, S.E., and Renard, J., 2008, Globally aligned photomosaic of
781 the Lucky Strike hydrothermal vent field (Mid-Atlantic Ridge, 37 degrees 18.50 ` N):
782 Release of georeferenced data, mosaic construction, and viewing software:
783 GEOCHEMISTRY GEOPHYSICS GEOSYSTEMS, v. 9, doi: 10.1029/2008GC002204.

784 Escartín, J., Soule, S.A., Cannat, M., Fornari, D.J., Düşünür, D., and Garcia, R., 2014, Lucky
785 Strike seamount: Implications for the emplacement and rifting of segment-centered
786 volcanoes at slow spreading mid-ocean ridges: Geochemistry, Geophysics,
787 Geosystems, v. 15, no. 11, p. 4157–4179, doi: 10.1002/2014GC005477.

788 Ferrini, V., and Tivey, M.K., 2012, ROV Jason 2 near-bottom multibeam bathymetry grids
789 from 6 vent fields in the Lau Back-arc Basin: Integrated Earth Data Applications
790 (IEDA), p. http://doi.org/10.1594/IEDA/100028.

791 Ferrini, V.L., Tivey, M.A., Carbotte, S.M., Martinez, F., and Roman, C., 2008, Variable
792 morphologic expression of volcanic, tectonic, and hydrothermal processes at six
793 hydrothermal vent fields in the Lau back-arc basin: Geochemistry, Geophysics,
794 Geosystems, v. 9, no. 7, p. Q07022, doi:10.1029/2008GC002047.

795 Fontaine, F.J., Cannat, M., Escartin, J., and Crawford, W.C., 2014, Along-axis hydrothermal
796 flow at the axis of slow spreading Mid-Ocean Ridges: Insights from numerical
797 models of the Lucky Strike vent field (MAR): Geochemistry, Geophysics,
798 Geosystems, v. 15, no. 7, p. 2918–2931, doi: 10.1002/2014GC005372.

799 Fontaine, F.J., Olive, J.A., Cannat, M., Escartin, J., and Perol, T., 2011,
800 Hydrothermally-induced melt lens cooling and segmentation along the axis of fast-

and intermediate-spreading centers: Geophysical Research Letters, v. 38, p. L14307, doi:10.1029/2011GL047798.

Fouquet, Y., Charlou, J.L., Costa, I., Donval, J.P., Radford-Knoery, J., Pellé, H., Ondréas, H., Lourenço, N., Ségonzac, M., and Tivey, M.K., 1994, A detailed study of the Lucky Strike hydrothermal site and discovery of a new hydrothermal site: Menez Gwen; Preliminary results of the DIVAI Cruise (5-29 May, 1994): InterRidge News, v. 3, no. 2, p. 14–17.

German, C.R., Baker, E.T., Connelly, D.P., Lupton, J.E., Resing, J., Prien, R.D., Walker, S.L., Edmonds, H.N., and Langmuir, C., 2006, Hydrothermal exploration of the Fonualei Rift and Spreading center and the Northeast Lau spreading center: Geochemistry, Geophysics, Geosystems, v. 7, no. 11, p. Q11022, doi:10.1029/2006GC001324.

German, C.R., Parson, L.M., and Team, H.S., 1996, Hydrothermal exploration near the Azores Triple Junction: tectonic control of venting at slow-spreading ridges: Earth and Planetary Science Letters, v. 138, p. 93–104.

German, C.R., Thurnherr, A.M., Knoery, J., Charlou, J.L., Jean Baptiste, P., and Edmonds, H.N., 2010, Heat, volume and chemical fluxes from submarine venting: A synthesis of results from the Rainbow hydrothermal field, 361N MAR: Deep-Sea Research I, v. 57, p. 518–527.

Gràcia, E., Charlou, J.L., Radford-Knoery, J.R., and Parson, L.M., 2000, Non-transform offsets along the Mid-Atlantic Ridge south of the Azores (38°N-34°N): Ultramafic exposures and hosting of hydrothermal vents: Earth and Planetary Science Letters, v. 177, p. 89–103.

Gràcia, E., Parson, L.M., Bideau, D., and Hekinian, R., 1998, Volcano-tectonic variability along segments of the Mid-Atlantic Ridge between the Azores platform and Hayes fracture zone: Evidence from submersible and high-resolution side-scan sonar data, *in* Mills, R.A. and Harrison, K. eds., Modern ocean floor processes and the geological record, Geological Society, London, p. 1–15.

Haase, K.M., Koschinsky, A., Petersen, T., Devey, C.W., German, C., Lackschewitz, K.S., Melchert, B., Seifert, R., Borowski, C., Giere, O., and Paulick, H., 2009, Diking, young volcanism and diffuse hydrothermal activity on the southern Mid-Atlantic Ridge: The Lilliput field at 9°33′S: Marine Geology, v. 266, p. 52–64.

Haymon, R.M., Macdonald, K.C., Benjamin, S.B., and Ehrhardt, C.J., 2005, Manifestations of hydrothermal discharge from young abyssal hills on the fast-spreading East Pacific Rise flank: Geology, v. 33, p. 153–156; doi: 10.1130/G21058.1.

Humphris, S.E., Fornari, D.J., Scheirer, D.S., German, C.R., and Parson, L.M., 2002, Geotectonic setting of hydrothermal activity on the summit of Lucky Strike seamount (37°17′N, Mid-Atlantic Ridge): Geochemistry, Geophysics, Geosystems, v. 3, no. 8, p. 10.1029/2001GC000284.

Humphris, S.E., and Kleinrock, M.C., 1996, Detailed morphology of the TAG active hydrothermal mound: Insights into its formation and growth: Geophysical Research Letters, v. 23, no. 23, p. 3443–3446.

842 Jamieson, J.W., Clague, D. a., and Hannington, M.D., 2014, Hydrothermal sulfide
843 accumulation along the Endeavour Segment, Juan de Fuca Ridge: Earth and
844 Planetary Science Letters, v. 395, p. 136–148, doi: 10.1016/j.epsl.2014.03.035.

845 Karson, J.A., and Brown, J.R., 1988, Geologic setting of the Snake Pit hydrothermal site:
846 an active vent field on the Mid-Atlantic Ridge: Marine Geophysical Researches, v. 10,
847 p. 91–107.

848 Kelley, D.S., Delaney, J.R., and Juniper, S.K., 2014, Establishing a new era of submarine
849 volcanic observatories: Cabling Axial Seamount and the Endeavour Segment of the
850 Juan de Fuca Ridge: Marine Geology, v. 352, p. 426–450, doi:
851 10.1016/j.margeo.2014.03.010.

852 Kleinrock, M.C., Humphris, S., and Thompson, G., 1993, Relations between volcanism,
853 tectonism and hydrothermalism along the TAG segment of the Mid-Atlantic ridge:
854 WHOI.

855 Klinkhammer, G., Rona, P., Greaves, M., and Elderfield, H., 1985, Hydrothermal
856 manganese plumes in the Mid-Atlantic Ridge rift valley: Nature, v. 314, p. 727–731.

857 Lalou, C., Brichet, E., and Lange, J., 1989, Fossil hydrothermal sulfide deposits at the
858 Galapagos Spreading Centre near 85°00 West: geological setting, mineralogy and
859 chronology: Oceanologica acta, v. 12, no. 1, p. 1–8.

860 Langmuir, C., Humphris, S., Fornari, D., Van Dover, C., Von Damm, K., Tivey, M.K.,
861 Colodner, D., Charlou, J. -l., Desonie, D., Wilson, C., Fouquet, Y., Klinkhammer, G., and
862 Bougault, H., 1997, Hydrothermal vents near a mantle hot spot: the Lucky Strike
863 vent field at 37°N on the Mid-Atlantic Ridge: Earth and Planetary Science Letters, v.
864 148, p. 69–91.

865 Lupton, J., 1990, Water column hydrothermal plumes on the Juan de Fuca Ridge: Journal
866 of Geophysical Research, v. 95, no. B8, p. 12829–12842.

867 Marcon, Y., Sahling, H., Borowski, C., dos Santos Ferreira, C., Thal, J., and Bohrmann, G.,
868 2013, Megafaunal distribution and assessment of total methane and sulfide
869 consumption by mussel beds at Menez Gwen hydrothermal vent, based on geo-
870 referenced photomosaics: Deep Sea Research Part I: Oceanographic Research
871 Papers, v. 75, p. 93–109, doi: 10.1016/j.dsr.2013.01.008.

872 Mittelstaedt, E., Escartín, J., Gracias, N., Olive, J.-A., Barreyre, T., Davaille, A., Cannat, M.,
873 and Garcia, R., 2012, Quantifying diffuse and discrete venting at the Tour Eiffel vent
874 site, Lucky Strike hydrothermal field: Geochemistry Geophysics Geosystems, v. 13,
875 no. 4, p. Q04008, doi: 10.1029/2011GC003991.

876 Murton, B.J., Klinkhammer, G., Becker, K., Briais, A., Edge, D., Hayward, N., Millard, N.,
877 Mitchell, I., Rousse, I., Rudnicki, J.W., Sayanagi, K., Sloan, H., and Parson, L., 1994,
878 Direct evicence for the distribution and occurrence of hydrothermal activity
879 between 27°N -30°N on the Mid-Atlantic Ridge: Earth and Planetary Science Letters,
880 v. 125, p. 119–128.

881 Murton, B.J., Redbourn, L.J., German, C.R., and Baker, E.T., 1999, Sources and fluxes of
882 hydrothermal heat, chemicals and biology within a segment of the Mid-Atlantic
883 Ridge: Earth and Planetary Science Letters, v. 171, p. 301–317.

884 Olafsson, J., Honjo, S., Thors, K., Stefansson, U., Jones, R.R., and Ballard, R.D., 1989, Initial
885 observations, bathymetry and photography of a geothermal site on the Kolbeinsey
886 Ridge, *in* Oceanography 1988 : JOA Mexico 88, p. 121–127.

887 Ondreas, H., Cannat, M., Fouquet, Y., Normand, A., Sarradin, P.M., and Sarrazin, J., 2009,
888 Recent volcanic events and the distribution of hydrothermal venting at the Lucky
889 Strike hydrothermal field, Mid-Atlantic Ridge: GEOCHEMISTRY GEOPHYSICS
890 GEOSYSTEMS, v. 10, doi: 10.1029/2008GC002171.

891 Ondréas, H., Cannat, M., Fouquet, Y., Normand, A., Sarradin, P.-M., and Sarrazin, J., 2009,
892 Recent volcanic events and the distribution of hydrothermal venting at the Lucky
893 Strike hydrothermal field, Mid-Atlantic Ridge: Geochemistry, Geophysics,
894 Geosystems, v. 10, no. 2, p. Q02006, doi:10.1029/2008GC002171.

895 Ondreas, H., Fouquet, Y., Voisset, M., and Radford-Knoery, J., 1997, Detailed study of
896 three contiguous segments of the Mid-Atlantic Ridge, South of the Azores (37°N to
897 38°30'N), using acoustic imaging coupled with submersible observations: Marine
898 Geophysical Researches, v. 19, p. 231–255.

899 Pedersen, R.B., Thorseth, I.H., Nygård, T.E., Lilley, M., and Kelley, D.S., 2010,
900 Hydrothermal Activity at the Arctic Mid-Ocean Ridges, *in* Rona, P., Devey, C.W.,
901 Dyment, J., and Murton, B. eds., Diversity of Hydrothermal Sytems on Slow
902 Spreading Ocean Ridges, p. 67–89.

903 Prados, R., Garcia, R., Gracias, N., Escartín, J., and Neumann, L., 2012, A novel blending
904 technique for underwater gigamosaicing: IEEE Journal of Oceanic Engineering, v.
905 37, no. 4, p. 10.1109/JOE.2012.2204152.

906 Scheirer, D.S., Fornari, D.J., Humphris, S.E., and Lerner, S., 2000, High-resolution seafloor
907 mapping using the DSL-120 sonar system: Quantitative assessment of sidescan and
908 phase-bathymetry data from the Lucky Strike segment of the Mid-Atlantic Ridge:
909 Marine Geophysical Researches, v. 21, p. 121–142.

910 Seher, T., Crawford, W.C., Singh, S.C., and Cannat, M., 2010, Seismic layer 2A variations in
911 the Lucky Strike segment at the Mid-Atlantic Ridge from reflection measurements:
912 Journal of Geophysical Research, v. 115, p. B07107, doi:10.1029/2009JB006783.

913 Singh, S.C., Crawford, W.C., Carton, H., Seher, T., Combier, V., Cannat, M., Canales, J.P.,
914 Düsünur, D., Escartín, J., and Miranda, J., 2006, Discovery of a magma chamber and
915 faults beneath a Mid-Atlantic Ridge hydrothermal field: Nature, v. 442, p. 1029–
916 1032.

917 Smith, D.K., and Cann, J.R., 1990, Hundreds of small volcanoes on the median valley floor
918 of the Mid-Atlantic Ridge: Nature, v. 344, p. 427–431.

919 Smith, D.K., Cann, J.R., and Escartín, J., 2006, Widespread active detachment faulting and
920 core complex formation near 13°N on the Mid-Atlantic Ridge: Nature, v. 443, p.
921 440–444, doi:10.1038/04950.

922 Thurnherr, A.M., Reverdin, G., Bouruet-Aubertot, P., St. Laurent, L.C., Vangriesheim, A.,
923 and Ballu, V., 2008, Hydrography and flow in the Lucky Strike segment of the Mid-
924 Atlantic Ridge: Journal of Marine Research, v. 66, p. 347–372.

925 Wilson, C., Charlou, J.-L., Ludford, E., Klinkhammer, G., Chin, C., Bougault, H., German, C.,
926 Speer, K., and Palmer, M., 1996, Hydrothermal anomalies in the Lucky Strike
927 segment on the Mid-Atlantic Ridge (37°17'N): Earth and Planetary Science Letters,
928 v. 142, p. 467–477.

929 Yeo, I., Searle, R.C., Achenbach, K.L., Le Bas, T.P., and Murton, B.J., 2011, Eruptive
930 hummocks: Building blocks of the upper ocean crust: Geology, v. 40, no. 1, p. 91–94,
931 doi: 10.1130/G31892.1.

932